WPS1-PR(18) 20825

B Geiger et al.

# Observation of anomalous impurity transport in low-density electron-heated W7-X plasmas based on laser-blow-off injections of iron and STRAHL+DKES modeling

Preprint of Paper to be submitted for publication in Nuclear Fusion

This work has been carried out within the framework of the EUROfusion Consortium and has received funding from the Euratom research and training programme 2014-2018 under grant agreement No 633053. The views and opinions expressed herein do not necessarily reflect those of the European Commission.

# Observation of anomalous impurity transport in Wendelstein 7-X

**B. Geiger[1], Th. Wegner[1], C. D. Beidler[1], R. Burhenn[1], B. Buttenschön[1], R. Dux[2], A. Langenberg[1], N. A. Pablant[3], T. Pütterich[2], Y. Turkin[1], T. Windisch[1], V. Winters[5], M. Beurskens[1], C. Biedermann[1], K. J. Brunner[1], G. Cseh[8], H. Damm[1], F. Effenberg[5], G. Fuchert[1], O. Grulke[1], J. H. Harris[7], C. Killer[1], J. Knauer[1], G. Kocsis[8], A. Krämer-Flecken[6], T. Kremeyer[5], M. Krychowiak[1], O. Marchuk[6], D. Nicolai[6], K. Rahbarnia[1], G. Satheeswaran[6], J. Schilling[1], O. Schmitz[5], T. Schröder[1], T. Szepesi[8], H. Thomsen[1], H. Trimino Mora[1], P. Traverso[4], D. Zhang[1] and the W7-X Team‡**

[1] Max-Planck-Institute for Plasma Physics, Wendelsteinstrasse 1, 17491 Greifswald
[2] Max-Planck-Institute for Plasma Physics, Boltzmannstrasse 2, 85748 Garching
[3] Princeton Plasma Physics Laboratory, Princeton, New Jersey 08543
[4] Auburn University, Auburn, Alabama 36849
[5] University of Madison, Madison, Wisconsin 53706
[6] Forschungszentrum Jülich, 52425 Jülich
[7] Oak Ridge National Laboratory, Oak Ridge, Tennessee 37830
[8] Wigner Research Center for Physics, Budapest 1121

**Abstract.** The transport of heavy impurities has been investigated at the Wendelstein 7-X stellarator during core electron root confinement (CERC) experiments. Iron atoms were injected via the laser blow-off technique and analyzed by VUV and X-ray spectrometers. The injected amount of iron does not change the global plasma parameters but yields strong enough line radiation for detailed studies based on the impurity transport code STRAHL. The latter is supplied with neo-classical diffusion and convection profiles from the Drift Kinetic Equation Solver (DKES) and has been embedded into a least-squares fit that searches for additional anomalous diffusion and convection profiles. While the resulting convection velocities agree within uncertainties with neo-classical theory, the anomalous diffusion profile is more than two orders of magnitude larger than the neo-classical one. This significant level of anomalous transport is possibly explained by turbulence. The shape of the anomalous diffusion profile resembles the shape of normalized temperature gradient length profiles and the absence of strong anomalous convection velocities agrees with this hypothesis.

‡ See the authors list in R. C. Wolf et al., Nucl. Fusion 57, 102020 (2017).

## 1. INTRODUCTION

Transport studies of heavy impurity ions are an active field in fusion research since the success of future power plants will depend crucially on the radiative cooling from highly charged ions. The latter maintain bound electrons even at high temperatures, emit intense line radiation and can be used to dissipate the heat from the alpha particles [1]. Since overly strong cooling would extinguish the burning plasma, reliable control of the impurity content and composition is needed. However, sound impurity control might be difficult as the different transport mechanisms, grouped into diffusive and convective contributions with neo-classical or anomalous origin, are not yet completely understood.

In stellarators, the neo-classical transport is particularly strong and becomes important in plasmas that feature high temperatures and sufficiently low collisionalities, $\nu^*$ (defined by the collision frequency of a given particle species, multiplied with its characteristic orbit time [2]). If not interrupted often enough by collisions, electrons and ions that are trapped in magnetic helical wells experience un-balanced drifts and move radially. These drifts are not intrinsically ambipolar and a radial electric field, $E_r$, must develop. In case of a stronger drift of electrons than of ions, a positive (outwards-directed) radial electric field appears (electron-root confinement) and in presence of a stronger ion-drift, a negative electric field appears (ion-root confinement). The electric field reduces the radial neo-classical diffusion through an additional and charge-independent poloidal $\vec{E_r} \times \vec{B}$ rotation (with $\vec{B}$ the magnetic field vector). In addition, $E_r$ contributes to the radial convection velocity. The energy gain or loss of a given particle in presence of $E_r$ results in an additional thermodynamic force, which can be found in the kinetic equation describing the particle flux, $\Gamma$, of a given particle species and charge stage [3]:

$$\Gamma = -\nabla n \cdot D_{11} + n \cdot \underbrace{(D_{11}\, q\, E_r/T - D_{12}\, \nabla\, T/T)} \tag{1}$$

$$\Gamma = -\nabla n \cdot D_{\mathrm{nc}} + n \cdot \qquad\qquad v_{\mathrm{nc}} \tag{2}$$

Here, $n$ and $T$ are a given species' charge stage density and temperature, $D_{11}$ and $D_{12}$ are elements of the neo-classical transport-coefficient matrix and $\nabla$ denotes the radial derivative. The second term in equation (1) can be expressed by a convection velocity ($v_{\mathrm{nc}}$) that depends on $q\, E_r$. For highly charged impurity ions this term is particularly strong and points outwards for $E_r > 0$ and inwards for $E_r < 0$.

High-performance plasmas with ion temperatures comparable to the electron temperature feature pure ion-root confinement and are expected to exhibit an inward-directed heavy impurity convection. This could lead to an undesired accumulation of impurities as observed at Wendelstein 7-AS [4]. However, recent theoretical findings predict impurity screening in a mixed collisionality regime at high ion temperatures [5]. Moreover, the anomalous impurity transport caused by turbulence might help avoiding accumulation. Turbulent impurity transport can be described by ordinary Fickian diffusion, has no strong mass or charge dependence ($\vec{E} \times \vec{B}$ driven) and features only

small anomalous convection velocities [6]. In tokamaks enhanced turbulent impurity transport is routinely observed during central electron cyclotron resonance heating (ECRH) and is used as a tool for accumulation avoidance [7]. In stellarators, however, turbulence-induced impurity transport was difficult to identify until now since the neo-classical transport was overwhelmingly strong and dependent on the background plasma profiles. A reduced tendency for impurity accumulation has, e.g., been observed in the LHD experiment when applying strong and central ECRH or NBI [8] but it is not clear whether this effect is due to a modification of the radial electric field (neo-classical transport) or caused by enhanced anomalous diffusion.

In contrast to most previous experiments, the magnetic field structure of Wendelstein 7-X (W7-X) [9, 10] is optimized for low neo-classical transport. The relative impact of anomalous transport can, therefore, be addressed much easier. In fact, results from the first operational phase of W7-X in 2016 suggest the presence of a strong diffusion of argon ions [11]. This observation is in line with our findings from the second operational phase in 2017. Radial impurity diffusion profiles are more than two orders of magnitude larger than the neo-classical ones.

This paper is structured as follows. First, the experimental setup and measurements of impurity line emissions are discussed in section 2. Section 3 provides a description of the modeling tools applied, consisting of DKES [12] used to infer neo-classical diffusion and convection profiles, STRAHL [13] needed for synthetic measurements of the impurity line radiation and impurity transport simulations and KN1D [14] applied to determine neutral background density profiles for STRAHL. In section 4, a least-squares fitting routine is introduced that allows inferring anomalous diffusion and convection profiles by minimizing the difference between measurements and STRAHL predictions. The impact of measurement- and modeling-uncertainties on the STRAHL results is addressed in section 5 and finally, a discussion and summary are given in sections 6 and 7.

## 2. EXPERIMENTAL SETUP

Experiments have been performed in the standard magnetic field configuration of W7-X (labeled EIM [15]) using hydrogen as main plasma species and up to 6 MW of ECRH power. Figure 1 shows time traces of a representative experiment with the ECRH heating power (a), the plasma stored energy [16] and the line-averaged density [17] (b). In figure 1c are shown the normalized emissivities of a Fe XXIII line ($Fe^{22+}$), a Fe XXV line ($Fe^{24+}$) and a Fe spectrum collected by a fast camera in the visible range (mainly Fe I and Fe II, according to NIST [18]). The increase of the line emissions at 0.96 s is due to the dedicated injection of iron atoms from a newly installed laser blow-off (LBO) system [19]. While clear Fe signals are observed after the LBO injection, no effect is seen on the plasma stored energy or density. This demonstrates that the injected amount of impurities does not perturb the background plasma and permits the assumption of constant diffusion, convection and kinetic profiles within the time range of the LBO

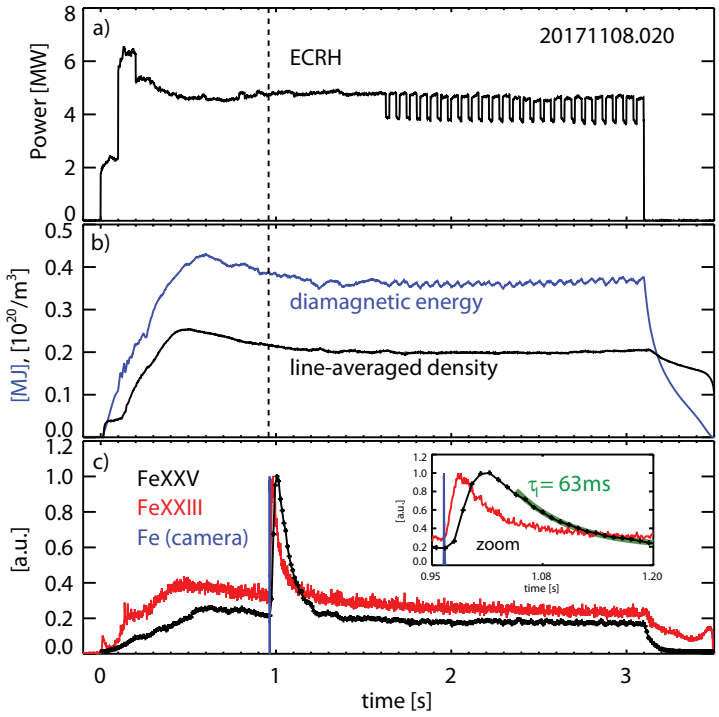


**Figure 1.** Representative time traces of experimental program 20171108.020, showing the ECRH power and gas flux (a), the plasma stored energy and line-averaged density (b) and emissivities of Fe spectral lines (c) occurring after the LBO injection at 0.96 s. An exponential decay is fitted to the Fe XXV line in (c) which yields an impurity transport time of $\tau_I$=63 ms. From 1.6 s on, one gyrotron of the ECRH system is modulated for heat pulse-propagation studies which are not discussed here.

injection.

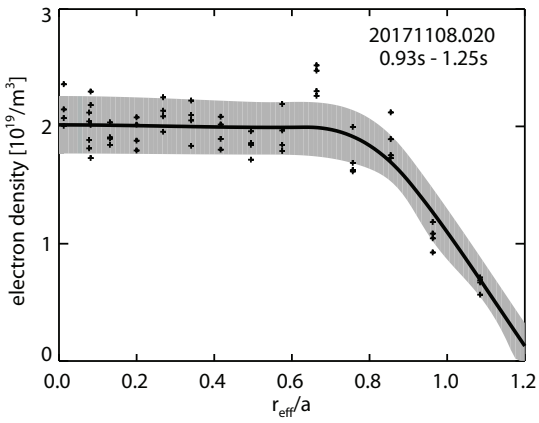


**Figure 2.** Electron density profile as a function of the normalized effective radius ($r_{\rm eff}/a$) between 0.95 s and 1.25 s. The thick lines represent a spline fit to the data. The shaded area indicates the measurement uncertainties.

Figure 2 shows profiles of the electron density for four time points between 0.95 and 1.25 s as a function of the normalized effective radius, $r_{\rm eff}/a$, where a is the minor radius and $r_{\rm eff} = \sqrt{\langle A\rangle/\pi}$, with $\langle A\rangle$ the average poloidal flux-surface area. The solid lines in

figure 2 correspond to a spline-function that will serve as input for the modeling tools, described in section 3 and the shaded areas indicate measurement uncertainties. The shape of the electron density profile is determined by the Thomson scattering diagnostic [20, 21]. Its height is based on a cross-calibration with the interferometry measurement [17] since the absolute calibration of the Thomson diagnostic was lost due to laser misalignment.

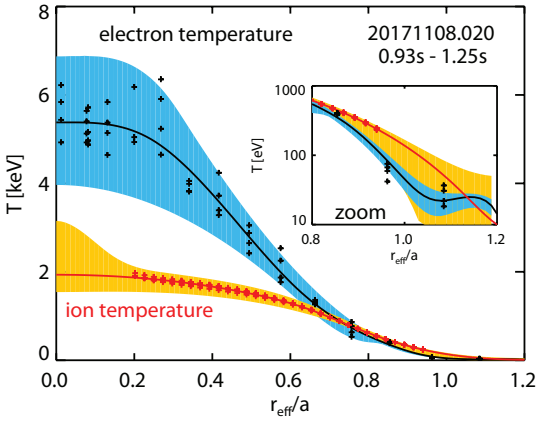


**Figure 3.** Electron temperature and ion temperature profiles between 0.95 s and 1.25 s. The thick lines represent a spline fit to the data. The shaded areas illustrate the measurement uncertainties.

The electron temperature profile from Thomson scattering is plotted in figure 3. It exhibits large gradients and reaches up to 6 keV in the center, explained by the strong on-axis ECRH power applied during the experiment. The ion temperature profile, plotted in red, is significantly lower and more flat than the electron temperature, given the weak thermal coupling between electrons and ions during low density experiments. The ion temperature profile originates from a profile-inversion of data from the X-ray Imaging Crystal Spectrometer (XICS) [22] which measures the Doppler broadening of an argon emission line.

The Doppler shift of this argon emission line yields additional information on the poloidal plasma rotation profile [23], which can be related to the $\vec{v} \times \vec{B}$ velocity via the force balance equation [24] and thus provides information on the radial electric field, $E_r$. Figure 4 shows in blue a reconstructed $E_r$ profile from XICS which is positive in the plasma center (electron-root) and becomes negative (ion-root) towards the edge. This behavior is typical of so-called core-electron-root confinement (CERC [25]) plasmas and is expected in presence of strong on-axis ECRH and low densities. In the scrape-off-layer (SOL, $r_{\mathrm{eff}}/a > 1$) and edge region, data from the reflectometry diagnostic is available (red crosses). This diagnostic analyzes the group velocity of density fluctuations that move with the plasma. The positive values of $E_{\mathrm{r}}$ in the SOL are due to the fast parallel flux of electrons into the divertor region, leaving the positively charged ions behind.

Neither the $E_{\mathrm{r}}$ profile, nor the kinetic profiles appear to be affected within measurement uncertainties by the LBO at 0.96 s, likely explained by the low number of

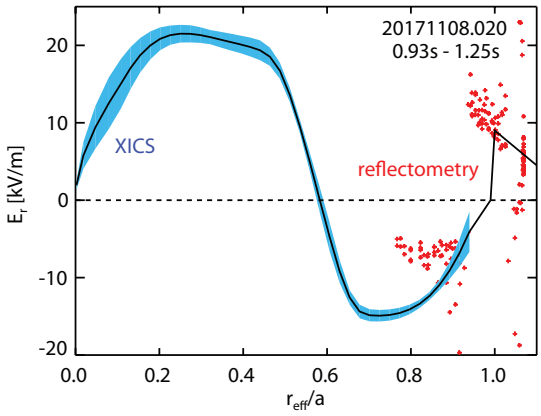


**Figure 4.** Radial electric field as measured by the XICS and reflectometry diagnostics. The estimated random uncertainty of the XICS measurements due to photon statistics is illustrated by the area shaded in blue.

iron atoms injected ($< 10^{17}$). The glass target of the LBO system was coated with a 5 $\mu$m thick layer of iron, which has been ablated by a 1 Joule Nd:YAG laser with a spot diameter of 4 mm. This correspond to about $10^{17}$ ablated particles of which a certain fraction will get ionized along the path to the plasma and then deflected by the magnetic field. The glass target is held by the multi-purpose manipulator [26] at a distance of 63 cm to the last closed flux surface.

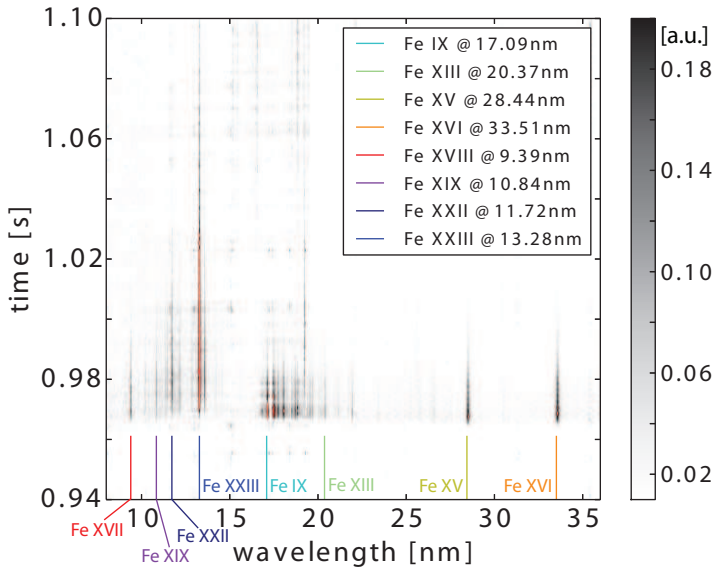


**Figure 5.** VUV-spectrum (HEXOS) as a function of time from which spectra before the LBO pulse (20 ms) have been subtracted. The color-coded vertical lines highlight the emissions lines, considered here.

Data from two spectrometers is used to analyze radiation from the injected impurities. First, data from the High-Efficiency eXtreme ultraviolet Overview Spectrometer (HEXOS) [27, 28] is applied, which covers the spectral range between

2.5 nm and 160 nm and provides access to lower ionization stages. Example spectra as a function of time are given in figure 5. To plot the net time evolution of the Fe lines, spectra from the time range 20 ms before the LBO pulse have been subtracted. Several Fe lines appear in the HEXOS data after the impurity injection of which eight lines have been selected for further analysis (color-coded in figure 5).

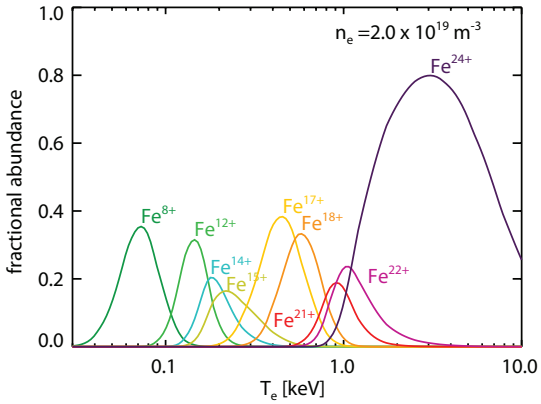


**Figure 6.** Fractional abundance assuming corona equilibrium (no radial transport) for selected charge stages as a function of the electron temperature.

Each line corresponds to a different ionization stage that is expected to radiate within a given temperature range. The fractional abundances of the corresponding charge stages are plotted in figure 6 as a function of the electron temperature. While the low charge stages are expected at temperatures even below 100 eV, the higher ones might appear in the keV range. This permits one to obtain radially resolved information from the emission lines since the experimental temperature profile covers this range.

Secondly, spectral information is obtained from the High-Resolution X-ray Imaging Spectrometer (HR-XIS) [29, 30] which monitors the helium-like iron emission (Fe XXV) at about 0.19 nm. The HR-XIS diagnostic uses a crystal and a CCD camera with 195 x 1475 pixels. Pixels in the vertical direction contain $r_{\mathrm{eff}}$ information, i.e. correspond to 1475 different vertical views with the upper and lower boundaries shown in figure 7a in red. Pixels in the horizontal direction contain wavelength information and cover the spectral range of the main Fe XXV excitation lines (w,x,y,z) as indicated in figure 7b, as well as dielectronic and inner shell excitation satellite lines. For the analysis performed here, we define three regions of interest on the chip (see colored boxes in figure 7b) which cover the w-line at different vertical positions. The corresponding average viewing geometries are given in figure 7a and labeled (I),(II) and (III).

Thanks to the high time-resolution of both spectrometers (1 ms for the HEXOS system and 10 ms for the HR-XIS system), the temporal evolution of different ionization stages of iron can be analyzed. Figure 1 already showed the temporal evolution of the Fe XXIII line (HEXOS) and the Fe XXV line (HR-XIS, view (I)). The evolution of all spectral lines is plotted in figure 8. The HR-XIS data has been normalized relative to the central line of sight (I) and the data from the HEXOS system has been normalized

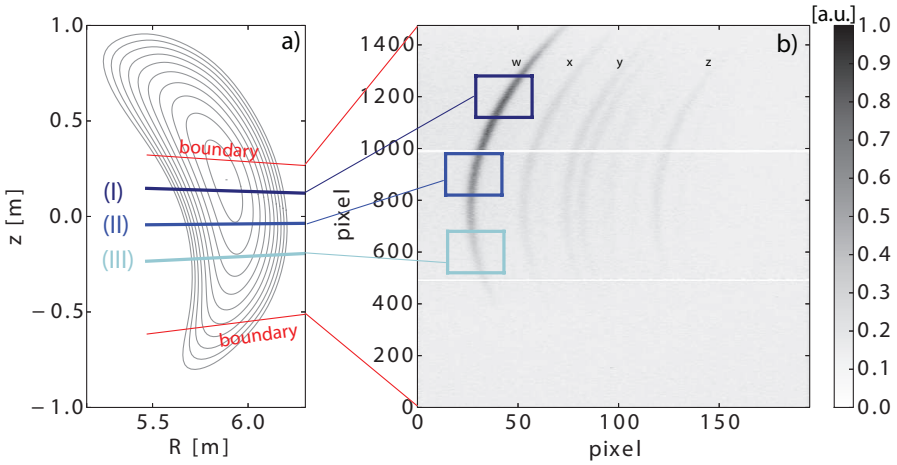


**Figure 7.** a) Poloidal cross section of W7-X at the toroidal angle of the HR-XIS diagnostic, showing flux surfaces of the standard magnetic field configuration. The boundary of the detector view is plotted in red and the three lines of sight defined in (b) are illustrated in blue. b) Raw detector image of the HR-XIS diagnostic showing Fe emission lines during exp. program 20171108.020 and three regions of interest, used to define specific lines of sight.

individually since a reliable calibration is not yet available. The lower ionization stages in figure 8 appear prior to the higher stages. This is well explained by the movement of the ablated Fe cloud from cold regions (near the plasma edge) to hot regions. The first decay phase of the lower ionization stages is due to the inward movement and further ionization to higher charge stages. Then, a slower decay should appear on the so-called transport time, $\tau_{\mathrm{I}}$ [19], which is, however, often obscured for the very low ionization stages due to noise in the data. In contrast, the Fe XXV line ($Fe^{24+}$) exhibits only the slow decay since this helium like stage appears in the core and further population of the hydrogen like stage is unlikely. Even at high electron temperatures of about 6 keV, the ionization rate of $Fe^{24+}$ into $Fe^{25+}$ is smaller than the back-transition by recombination (see figure 11). Thus $\tau_{\mathrm{I}}$=63 ms can be inferred from the decay of the Fe XXV line, as shown in figure 1.

The detailed modeling of the rise-time, the decay time and the relative intensities of the Fe lines will be discussed in the following.

## 3. MODELING USING DKES, STRAHL AND KN1D

### *3.1. DKES*

The Drift Kinetic Equation Solver (DKES) [12] is used to determine neo-classical diffusion and convection profiles. DKES solves the drift-kinetic equation using a monoenergetic and local ansatz. For a given magnetic field configuration, it returns data-base files with monoenergetic transport coefficients as a function of $r_{\mathrm{eff}}$, $\nu^*$ and $E_{\mathrm{r}}/(vB)$ with the particle velocity $v$ and the magnetic field strength $B$. From the monoenergetic transport coefficients, the neo-classical transport matrix can be obtained

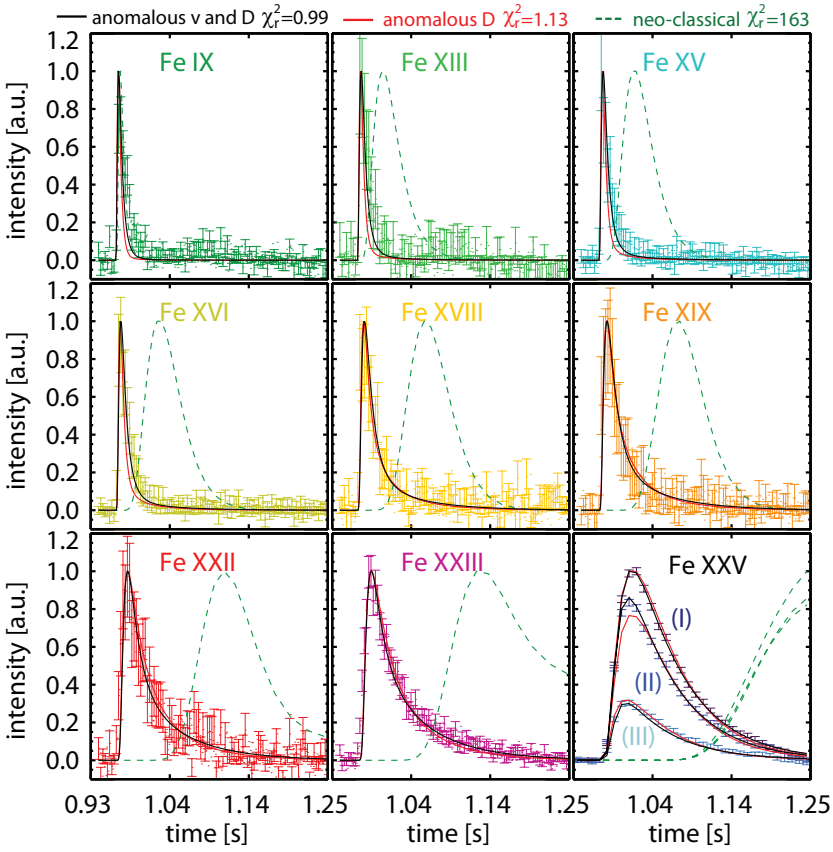


**Figure 8.** Time traces of eight different emission lines, as observed by HEXOS and the Fe XXV emission observed by HR-XIS at three different positions. The synthetic data illustrated with green dashed lines represents a STRAHL simulation based on neo-classical $D_{\rm nc}$ and $v_{\rm nc}$ profiles only. The simulation in black corresponds to the result when fitting the data with additional anomalous $D_{\rm a}$ and $v_{\rm a}$ profiles in STRAHL. The fitted data in red considers a neo-classical convection profile and an anomalous diffusion profile. The red lines are difficult to see since they are superimposed by the black ones.

by energy-convolution with a Maxwell distribution function. The first element of the transport matrix $D_{11}$ is the local diffusion coefficient, $D_{\rm nc}$. The local convection velocity, $v_{\rm nc}$, can be calculated from equation (1), i.e. $v_{\rm nc} = D_{11}\, q\, E_r/T - D_{12}\, \nabla T/T$.

Here, we use the measured kinetic and $E_{\rm r}$ profiles presented in section 2 to obtain the neo-classical transport matrix. In addition, we assume that the injected impurities do not affect the transport coefficients (i.e. that the Fe density is below the tracer-limit, discussed later). The calculated collisionality profiles, as well as the resulting neo-classical convection and diffusion profiles are plotted in figure 9 for several ionization stages. From the center to the SOL, the convection velocity drives impurities outwards, then becomes inward-directed and finally drives impurity ions outwards again. The strength of the neo-classical convection velocity increases with charge due to the charge-dependence of the thermodynamic force, related to $E_{\rm r}$. In contrast, the strength of the neo-classical diffusion profile scales inversely with charge, caused by the $1/q$ dependence

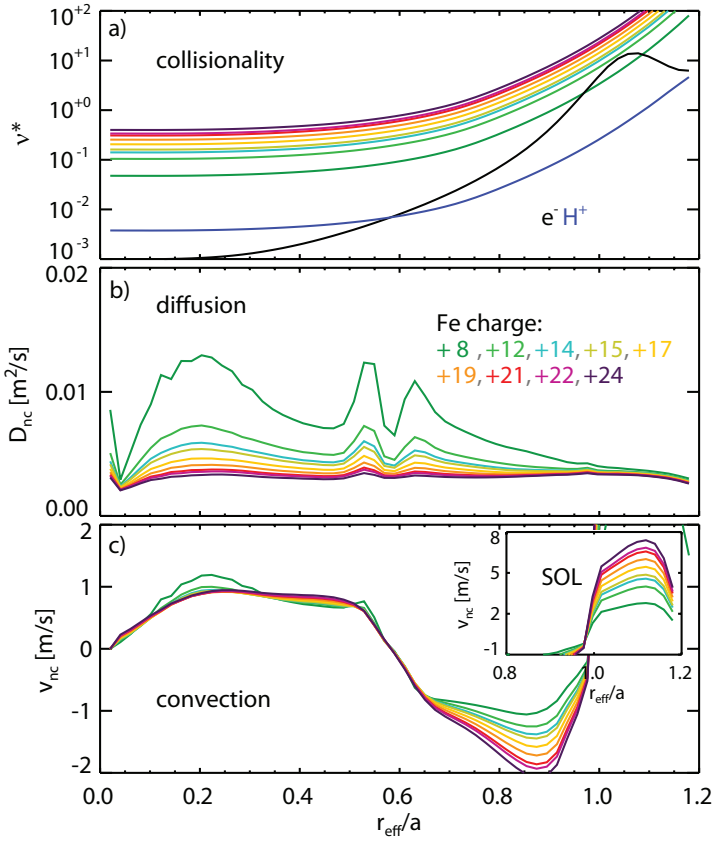


**Figure 9.** Radial profiles of the collisionality $\nu*$ (a), the neo-classical diffusion (b) and neo-classical convection velocity (c) from DKES for different ionization stages of iron.

of the curvature and gradient $B$ drifts that dominate neo-classical transport. The obtained neo-classical diffusivities are relatively low. This results from the optimization of W7-X with respect to neo-classical transport and from the further reduction of $D_{\mathrm{nc}}$ in presence of the $\vec{E}_{\mathrm{r}} \times \vec{B}$ induced poloidal rotation.

### *3.2. KN1D*

The KN1D code [14] has been applied to calculate neutral background densities which can affect the charge stage distribution of Fe via charge-exchange collisions. KN1D is a 1D code that calculates the $H_2$ gas flux from the wall, the dissociation of $H_2$ molecules and finally the propagation of H in the plasma considering ionization and charge-exchange reactions. Here, KN1D is supplied with the same kinetic profiles as used in DKES. Additionally, KN1D would require the hydrogen gas density and temperature (pressure) close to the wall. Since this information is not available, we consider an arbitrary density ($1 \times 10^{17}\,\mathrm{m}^{-3}$) and wall temperature (3 eV) and scale the resulting profiles to the edge-neutral density measured from filterscopes [31]. The latter observe a flux of H-atoms between $10^{18}$ and $10^{21}$ particles per second and $\mathrm{m}^2$, depending on the 3D measurement location. The measured fluxes can be translated into neutral densities

by considering an edge neutral temperature of 3 eV (the Franck-Condon dissociation energy of $H_2$), i.e. a velocity of 24 km/s for hydrogen. Figure 10 shows resulting neutral density profiles from KN1D in gray dashed lines which have been scaled to an edge density of $4\times10^{13}$ and $4\times10^{16}\,\mathrm{m}^{-3}$ (according to the measured fluxes of $10^{18}$-$10^{21}/\mathrm{s/m}^2$). The impact of the high and low density will be discussed in section 5. For the modeling results discussed in section 4, the intermediate density profile (black) will be considered.

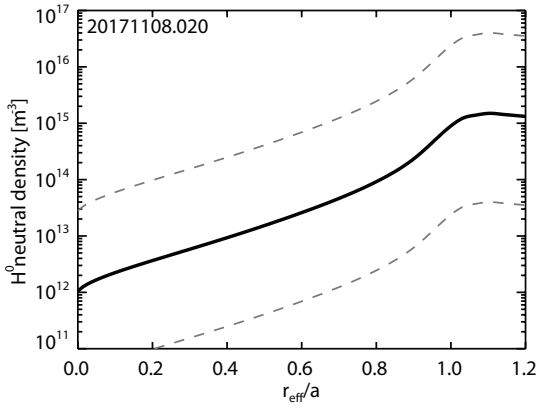


**Figure 10.** Neutral density profiles of H from KN1D as a function of $r_{\mathrm{eff}}/a$. The thin, dashed lines represent the uncertainties, considered during the sensitivity study presented in section 5.

### *3.3. STRAHL*

The STRAHL code [13] is applied to calculate emissivity profiles of selected spectral lines. STRAHL solves the impurity transport equation as a function of the impurity charge stage and effective radius (1D calculation) and requires kinetic profiles (optionally also the neutral density profiles), the device geometry, time traces of the impurity source and atomic data. Moreover, a parameter file is needed that contains e.g. settings for the impurity source location, the time-steps of the simulation or information on the plasma species. One can also specify anomalous diffusion and convection profiles while the neo-classical profiles are typically calculated within STRAHL by a built-in and tokamak-specific neo-classical module (NEOART). For W7-X, we added the possibility to consider the charge-dependent $D_{\mathrm{nc}}$ and $v_{\mathrm{nc}}$ profiles from DKES, similar to the approach described in [32].

The kinetic profiles input to STRAHL are the spline functions, already discussed in section 2. As radial coordinate for those profiles in STRAHL, the normalized volume, $\rho_{\mathrm{vol}}$ is used:

$$\rho_{\mathrm{vol}} = \sqrt{\frac{V}{2\pi R}} \tag{3}$$

Here, $V$ is the volume enclosed by a given flux surface and $R = 5.5\,\mathrm{m}$ the major radius of the device. The $\rho_{vol}$ coordinate permits an accurate description of the

radial impurity fluxes and can be directly compared with (is actually equal to) the $r_{\rm eff}$ coordinate on which the W7-X data is mapped.

The distance between the last closed flux surface and the plasma-vessel (wall) has been set to 10 cm in the simulation. This implies that the maximum $r_{\rm eff}/a$ value considered in STRAHL is about 1.2. When modeling the flux of particles in the SOL, STRAHL considers a connection length, $L_c$, and parallel flow velocity into the divertor. The flow velocity is set to a mach-number of 0.2, while $L_c$=250 m is used according to [33]. The impact of the choice of $L_c$ and the mach-number will be discussed in section 5. The divertor and the first wall define two sinks of particles in the simulation from which recycling has been turned off since Fe does not recycle.

The position of the LBO source in STRAHL is at the actual target positions (63 cm distance to the last closed flux surface) from which Fe atoms are launched with an energy of 20 eV, as inferred from a time of flight analysis of fast camera data. Data from the fast camera is also considered to describe the temporal shape of the impurity source function (see figure 1) while the total number of particles has been set to $10^{17}$, as estimated in section 2 as an upper boundary. The start of the LBO injection in STRAHL is defined 1.5 ms prior to the rise of the observed Fe IX emission. This is coarse but cannot be improved further since the timing of the laser and the time-base of the fast camera (seeing the Fe emission in the visible spectral range) are even worse. The impact of this timing uncertainty on the modeling result will be discussed in section 5 (Here, it should be noted that the time-bases of the HEXOS and HR-XIS systems are accurate to 1 ms).

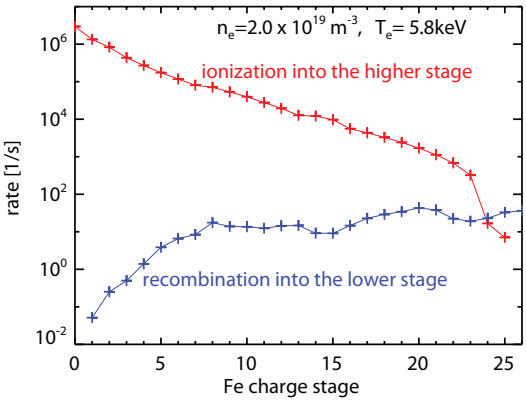


**Figure 11.** Ionization and recombination rates used in STRAHL as a function of the charge stage for an electron temperature of 5.8 keV and an electron density of $2 \times 10^{19}/m^3$.

The transport equations for a given ionization stage are coupled via the ionization, recombination and charge exchange rates into and from neighboring stages. Here we use existing temperature- and density-dependent database files from ADAS [34], labeled scd89_fe for ionization, acd85_fe for recombination and ccd89_fe for charge exchange. An example of the applied recombination and ionization rates is plotted in figure 11. Moreover, photo-emission coefficient 'PEC-files' (as a function of density and temperature) are required for the calculation of specific line emissions. The latter have

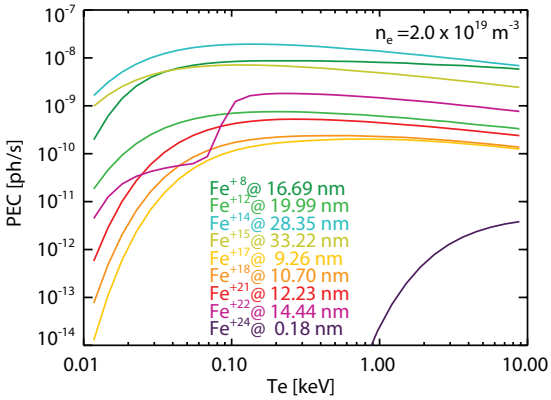


**Figure 12.** Photo emission coefficients considered by STRAHL as a function of the electron temperature, assuming an electron density of $2 \times 10^{19}/\mathrm{m}^3$.

recently been calculated using a modern set of ADAS codes [35] and are illustrated in figure 12 for the spectral lines analyzed here. The PEC values depend only weakly on the electron density and do not strongly change at electron temperatures above 100 eV (except for the Fe XXV line).

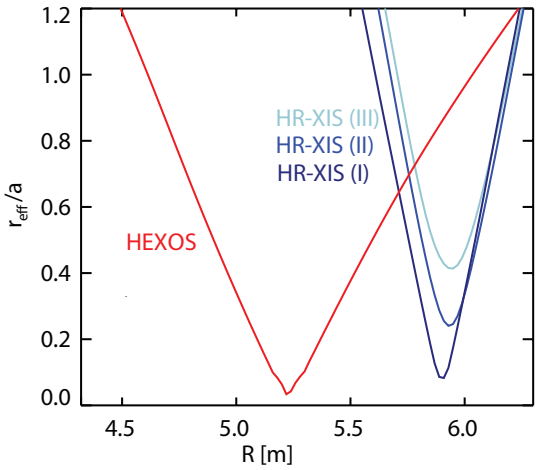


**Figure 13.** Normalized effective radius, $r_{\mathrm{eff}}/a$, present along the lines of sight of the HEXOS and HR-XIS spectrometers as a function of the major radius.

The output of STRAHL contains radial emissivity profiles as a function of time. These profiles need to be line-integrated per time-step before a comparison with the experimental data is possible. For the line-integration, $r_{\mathrm{eff}}/a$ values along the path of a given line have been determined using VMEC [36] equilibrium calculations and extrapolation into the SOL. Figure 13 illustrates radial profiles of those $r_{\mathrm{eff}}/a$ values for the HEXOS and HR-XIS views. The HEXOS view has a longer path through the plasma than the HR-XIS views since it crosses the triangular shaped plane and not the slim bean-shaped plane. In addition, the HEXOS view reaches the plasma center ($r_{\mathrm{eff}}/a \approx 0$) while the HR-XIS views exhibit a more or less pronounced off-axis character.

## 4. MODELING RESULTS

To check whether the experimental data can be modelled by the assumption of neo-classical transport, the $D_{\mathrm{nc}}$ and $v_{\mathrm{nc}}$ profiles from DKES were input to STRAHL. Hereby, an additional ad-hoc anomalous diffusion of $0.1\,\mathrm{m}^2/\mathrm{s}$ was added in the SOL to ensure that the injected Fe-ions reach the confined region sufficiently fast. Figure 8 shows the evolution of emissivities from this neo-classical simulation by green, dashed lines. The predicted decay of the emission lines from the low charge stages is too slow compared with the experimental data, the higher charge stages appear with a clear delay and their rise-times are too slow. In particular the time-delay, but also the rise and decay times clearly demonstrate that the injected iron particles move much quicker into the plasma center than expected from neo-classical theory. Thus, it can already be concluded, here, that anomalous transport is additionally present in the experiment.

To obtain more details on this anomalous transport, least-squares fitting is applied similar to the approaches described in [37, 38, 39]. The fitting algorithm modifies anomalous $D_{\mathrm{a}}$ and $v_{\mathrm{a}}$ profiles in STRAHL and searches for parameters that minimize the sum of squared residuals, $\mathcal{X}^2$:

$$\mathcal{X}^2 = \sum_i \left( \frac{I[i] - S[i]}{\sigma[i]} \right)^2 \tag{4}$$

Here the sum goes over $i$ data points $I$[i], $S$[i] is the model function (STRAHL) and $\sigma$[i] are the measurement uncertainties. The latter are considered to be the square root of the measurement values before normalization (photon statistics) plus an estimate for the readout noise. In addition, the data of the HR-XIS signal has been weighted by a factor of $\sqrt{30}$ since 30 times more data points are available from the HEXOS system. The temporal resolution of HEXOS is 10-times higher (1 ms instead of 10 ms) and three times more spectral lines/views are used. Without this extra-weighting, the few HR-XIS data points would not be considered sufficiently by the fit.

The profiles to be modified in STRAHL are parametrized with four spline-knots for $D_{\mathrm{a}}$ and three spline-knots for $v_{\mathrm{a}}$. During the fitting process, an initial fit-run is performed with free knot-values and fixed knot-positions. The result of this fit-run serves as initial guess for a second fit-run with both, free spline-knot positions and values (except for the innermost knot-position, fixed at $r_{\mathrm{eff}}/a$=0.1). Outside the innermost and outermost knots, the profiles are continued flat. The fit is allowed to move the spline-knots between $r_{\mathrm{eff}}/a$=0.1 and $r_{\mathrm{eff}}/a$=1.2 and will sort the knot-positions before doing the spline-interpolation. The knot-values for the $D_{\mathrm{a}}$ profile are constrained between $0\,\mathrm{m}^2/\mathrm{s}$ and $4\,\mathrm{m}^2/\mathrm{s}$ and the bounds of the convection knots are set to $\pm 3\,\mathrm{m/s}$. Constraining the knot-values limits the resulting spline values only in part since larger values can still be reached between the knots. As mentioned before, the position of the innermost spline-knot has been fixed to $r_{\mathrm{eff}}/a$=0.1 since information on the plasma core is limited. The slight off-axis geometry of the innermost HR-XIS view and the absence of lower ionization stages in the hot core (no HEXOS data) make conclusions for this region difficult.

The first fit-run is quick since only seven knot-values are modified and since we limit the number of fit-iterations to ten. For the second run, 12 free parameters are modified and about 100 iterations are required to converge. This involves a total number of 1300 STRAHL runs since derivatives for each free parameter (12 STRAHL runs) are calculated before coming to the next iteration step (+1). In total, about 20 minutes are required to obtain a fit-result, given that a single STRAHL run takes about 1 s on our computers (Intel Xenon E5, 2.8 GHz).

The evolution of spectral emissivities from the fit-result are plotted in figure 8 in black. The synthetic data agrees very well with the measurements, also indicated by a reduced $\mathcal{X}^2$ value of 0.99 ($\mathcal{X}^2_r = \mathcal{X}^2/N$, with $N$ the number of measurement points). Not only the evolution of all charge stages but also the relative intensities of the three HR-XIS views are recovered well by the fit. Only the decay of the lowest ionization stages is not matched perfectly since the emission of these lines appears close to the SOL (see figure 16) where the 3D structure of the island chain makes an accurate description challenging.

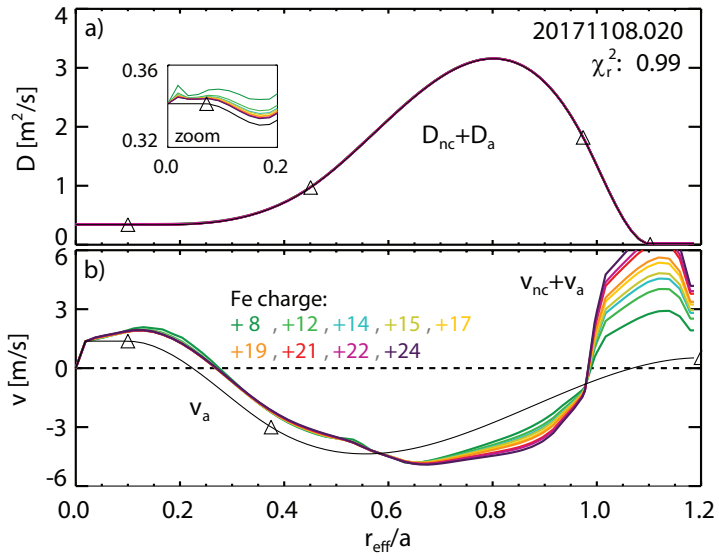


**Figure 14.** Diffusion and convection profiles as a function of $r_{\rm eff}/a$, obtained when fitting the data in figure 8. In black are given the anomalous profiles only with the spline-knot positions illustrated by triangles.

The corresponding $D$ ($D_{\rm nc} + D_{\rm a}$) and $v$ ($v_{\rm nc} + v_{\rm a}$) profiles from the fit are plotted in figure 14. In addition, the pure $D_{\rm a}$ and $v_{\rm a}$ profiles are illustrated with thin black lines and the spline-knots are indicated by triangles. The $D_{\rm a}$ profile is more than two orders of magnitude larger than the neo-classical expectation such that the neo-classical contribution is hardly visible and a zoom is needed. In contrast, the shape of the resulting $v_{\rm nc} + v_{\rm a}$ profile resembles the neo-classical case and the charge dependence can still be seen.

Figure 15 shows reconstructed Fe density profiles from this fit-result for various time-points on a semi-logarithmic scale. Shortly after the LBO pulse, the Fe density is

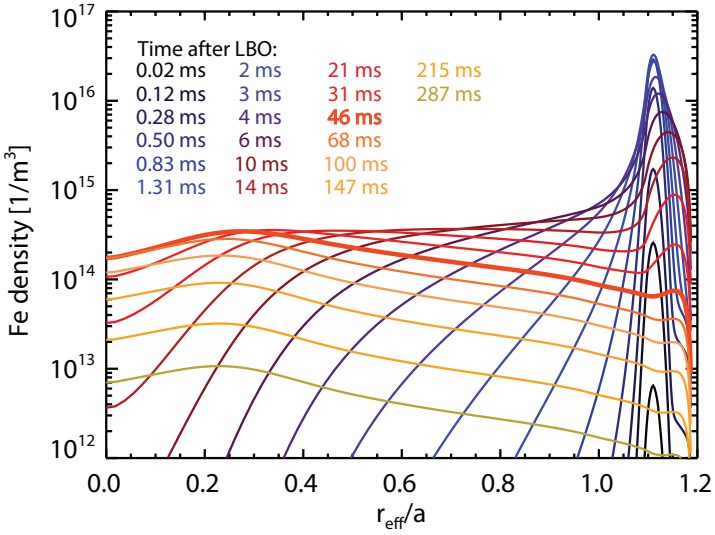


**Figure 15.** Radial Fe density profiles from STRAHL for different time-points.

peaked at $r_{\rm eff}/a$=1.1 where the incoming Fe neutrals get ionized. Then, the Fe cloud moves inwards and reaches the plasma center after about 20 ms. During this first phase, strong radial gradients appear such that diffusion can dominate the impurity flux. The observed time-delays and rise-times of the Fe radiation can thus be reproduced by the fit through the adjustment of the diffusion profile. Theoretically, also weak diffusivities and strong inward-directed convection velocities could explain the time-delays and rise-times. This would, however, be in contradiction with the measured decay-time of the high ionization stages, i.e. the observed transport time. The latter corresponds to the longest eigentime of the transport equation and is typically set by the lowest diffusivity (and or lowest $v$ values (negative ones)) in the profile. During the experiment analyzed here, the transport time is determined by the low diffusion close to the edge that acts like a valve releasing impurities into the divertor with $\tau_{\rm I}$=63 ms. This relatively short time scale cannot be matched by low diffusivities and strong negative convection velocities. The combined analysis of $\tau_{\rm I}$, the time-delay and the rise-time of the emission lines thus allows us to conclude without ambiguity that the anomalous transport is dominated by diffusion.

The second phase after the inward-movement of the density front is characterized by a constant logarithmic profile shape $\nabla log(n) = \frac{\nabla n}{n}$. At times, $t$, that are long compared with $\tau_{\rm I}$, the impurity density decays with $n \sim n_0(r)\, e^{-\frac{t}{\tau_{\rm I}}}$ at all radii, $r$. Thus, the impurity flux $\Gamma(r,t)$ [40, 41] can rewritten by

$$\Gamma(r,t) = -\frac{1}{r}\int_0^r \frac{\partial n(r',t)}{\partial t}\, r'\, dr' \sim +\frac{1}{r}\frac{e^{-\frac{t}{\tau_{\rm I}}}}{\tau_{\rm I}}\int_0^r n_0(r')\, r'\, dr' \tag{5}$$

and the ratio $\frac{\Gamma}{n}$ becomes independent of time:

$$\frac{\partial}{\partial t}\frac{\Gamma}{n} = 0 = -\frac{\partial}{\partial t}\frac{\nabla n}{n}\, D + \frac{\partial}{\partial t}\, v \tag{6}$$

Equation (6) has been obtained by rearranging equation (2) and applying the time derivative. Since we assume $D$ and $v$ to be constant in time, this implies that $\frac{\nabla n}{n}$ is constant in time, as well and explains the data in figure 15 where all profiles for $t > 46$ ms exhibit the same density peaking. The density peaking is closely related to the $v/D$ profile, which can be understood when rearranging equation (2):

$$\frac{\nabla n}{n} = v/D - \frac{\Gamma}{n\,D} \tag{7}$$

In case of equilibrium conditions ($\Gamma = 0$) or large $D$ values, the second term on the right side of equation 7 vanishes or becomes small, showing the close relation between $\frac{\nabla n}{n}$ and $v/D$.

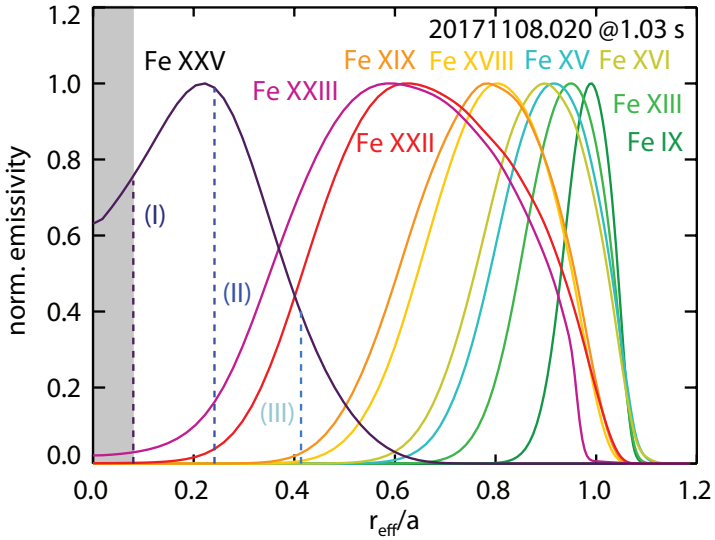


**Figure 16.** Radial emissivity profiles from STRAHL (normalized) as a function of $r_{\rm eff}/a$.

Experimentally, the density peaking $\frac{\nabla n}{n}$ can be accessed by the imaging spectrometer (HR-XIS), which probes the Fe XXV emission at three different positions. Figure 16 shows in black the modeled Fe XXV emission profile, together with vertical dashed lines for the minimum $r_{\rm eff}/a$ positions, reached by the three views. The fit finds a hollow Fe XXV emission profile in the center since view (I) exhibits only slightly stronger signals than view (II) (see figure 8) despite its longer path through the plasma (see figure 13). The hollowness of the Fe XXV emission profile is obtained by the fit through positive $v/D$ values in the center, i.e. positive $v$ values and relatively small $D$ values (see figure 14).

Outside $r_{\rm eff}/a$=0.2, the reconstructed Fe XXV emission profile decreases with radius in order to reproduce the weak signal from view (III). The negative slope of the Fe XXV emission profile translates into a negative density peaking outside $r_{\rm eff}/a$=0.2 which is obtained by the fit by assuming negative anomalous convection velocities.

This shows that the Fe XXV emission profile contains additional and valuable information on the $v$ and $D$ profiles. However, the information is limited to 0.1<

$r_{\rm eff}/a<0.6$ since the region inside $r_{\rm eff}/a$ =0.1 (gray shaded area in figure 16) is not accessed by the diagnostic and outside $r_{\rm eff}/a$ =0.6, radiation from Fe XXV is not expected. The PEC coefficient of the Fe XXV emission becomes relevant only above about 1 keV (see figure 12) which makes reconstructions of the full $v/D$ profile challenging. This also explains why we used only three spline-knots to parametrize $v_{\rm a}$. More spline knots might slightly reduce $\mathcal{X}^2$ but would also introduce unphysical oscillations.

Finally, it should be noted that the fit result presented here justifies the tracer-limit assumption [42], made when running DKES, i.e. ignoring the effect of the injected impurities on transport. Inside the confined region, the impurity density is well below $10^{15}/{\rm m}^3$ for all time-points. This is more than four orders of magnitude lower than the electron density and is low enough to be below the tracer-limit: $n\,Z^2 \ll n_e$, where $Z$ is the impurity charge and $n_e$ the electron density. Also in the SOL region, where the $n$ is higher (about $10^{16}/{\rm m}^3$) and $n_e$ lower, the tracer-limit approximation is still fulfilled since only low charge stages appear, such that $n\,Z^2/n_e$ remains below 0.05.

## 5. SENSITIVITY STUDY

The uncertainty of the profile reconstruction motivates a scan of about 120,000 STRAHL runs with modified $D_{\rm a}$ and $v_{\rm a}$ profiles to check for the existence of other minima in the $\mathcal{X}^2$ map, which may be missed by the fitting algorithm. For the scan, the profiles are described by three spline-knots with two fixed knot-positions at $r_{\rm eff}/a$=0 and 1.05. The third knot position in the middle is varied in 7 steps between $r_{\rm eff}/a$=0.2 and 0.9. Moreover, the outer two knot-values are modified within 7 steps between 0.1 ${\rm m}^2/{\rm s}$ and 2 ${\rm m}^2/{\rm s}$ for $D_{\rm a}$ and between -5 m/s and +5 m/s for $v_{\rm a}$. Thus, six parameters are scanned within 7 steps which results in a map of $7^6$ $\mathcal{X}^2_r$ values.

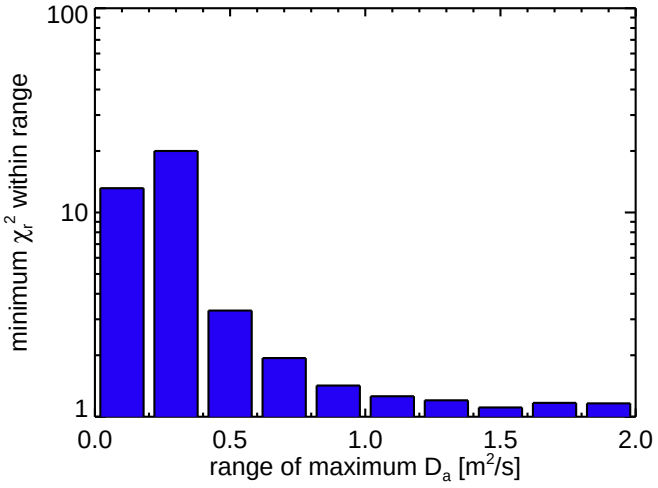


**Figure 17.** Minimum $\mathcal{X}^2_r$ within the range of maximum $D_{\rm a}$ values reached by the $D_{\rm a}$ profiles when performing the scan of $7^6$ STRAHL runs.

First, this map shows that there is no good solution ($\mathcal{X}_r^2$ <2) with an anomalous $D_\mathrm{a}$-profile having values uniformly below $1.0\,\mathrm{m}^2/\mathrm{s}$. Figure 17 illustrates the minimum values contained in the $\mathcal{X}_r^2$ map when selecting only profiles within a certain range of maximum $D_{\mathrm{a,\,max}}$ values. Clearly, the $\mathcal{X}^2$ values increase strongly when considering diffusion profiles with overall low values ($D_{\mathrm{a,\,max}} < 1\,\mathrm{m}^2/\mathrm{s}$). This shows that no solution exists with $D$ sufficiently low to agree with neo-classical theory. The observed short time-delays for the appearance of emission lines from the core (e.g. Fe XXV) cannot be modeled without strong anomalous transport.

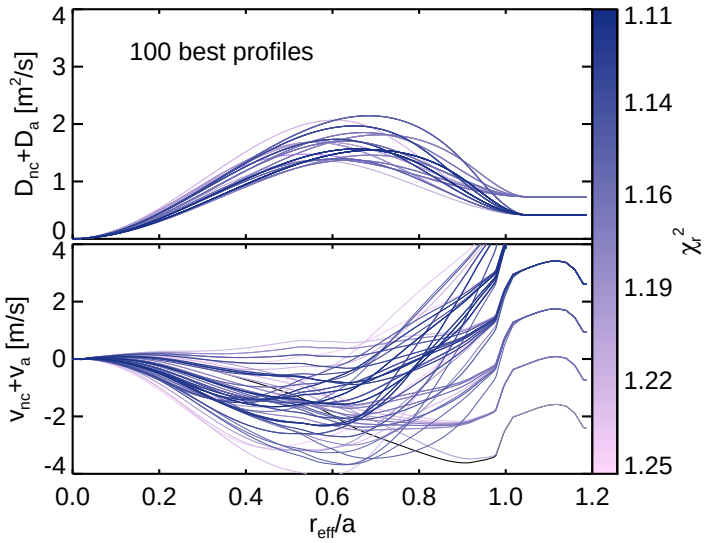


**Figure 18.** 100 radial $D_\mathrm{a}$ and $v_\mathrm{a}$ profiles with lowest $\mathcal{X}^2$ values from a scan of 120,000 STRAHL simulations.

Secondly, the scan result can be used to select the best fitting profiles. Figure 18 displays 100 anomalous $D_\mathrm{a}$ and $v_\mathrm{a}$ profiles that correspond to the lowest $\mathcal{X}_r^2$ values. The $\mathcal{X}_r^2$ values (see color-code) are not as low as when using the fitting algorithm (about 1.1 instead of 1.0) since here, the step sizes are finite and less spline-knots are used. Still, $\mathcal{X}_r^2$ values of 1.1 indicate a good representation of the data. The shape and height of the resulting $D_\mathrm{a}$ profiles are similar to the fit-results presented before and underline the increased $D$ values towards the edge region. The variation of $v$ profiles is strong and also seems to cover the case of a pure neo-classical convection velocity ($v_\mathrm{a} = 0$).

In fact, fitting the experimental data with the algorithm described above but forcing the anomalous convection to zero also yields a good representation of the data. The corresponding synthetic emissivities are illustrated in red in figure 8 and match well the data ($\mathcal{X}_r^2$=1.13). Only the evolution of view (II) of the HR-XIS system does not perfectly agree, explained by the difficulty for the fit to reproduce the negative peaking of the Fe XXV emission profile despite overall positive neo-classical convection velocities in the core. The corresponding $D$ profile is shown by the solid, red line in figure 19. The shape exhibits a minimum at $r_\mathrm{eff}/a$=0.4 which acts like a transport barrier and allows the fit to obtain centrally peaked density profiles. Towards the edge-region, the shape

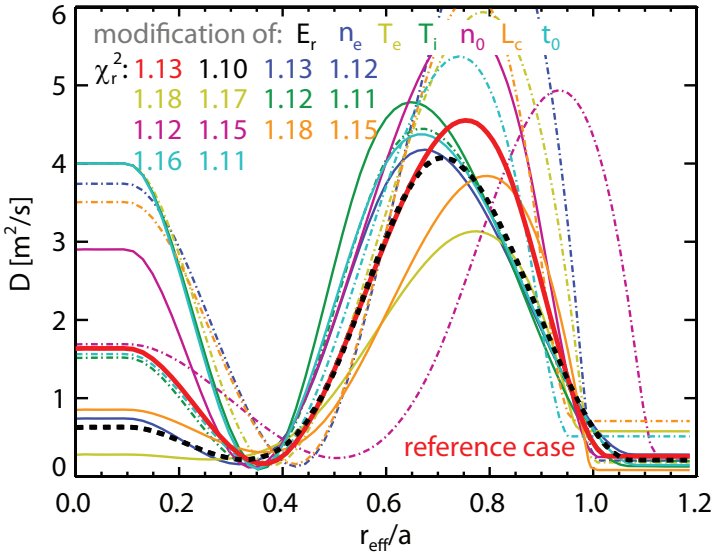


**Figure 19.** Anomalous $D_a$ profile obtained when fitting the data in figure 8 with $v_a$=0 (red). In addition, fit-results are plotted that correspond to modified input profiles and settings. The modified settings and profiles (reduced and increased ones) and the resulting $\mathcal{X}_r^2$ values are color-coded. The first $\mathcal{X}^2$ value of a given setting/profile corresponds to reduced settings/profiles (solid lines) while the second one corresponds to increased settings/profiles (dashed lines).

is similar to the fit-result discussed in section 4 while the maximum diffusion is about 50% higher.

The possibility of a pure neo-classical convection velocity profile has been further checked by 13 additional STRAHL fit-runs during which one given input profile or input setting has been modified. The impact of the $E_r$ profile on the DKES and STRAHL results has been investigated by running DKES iteratively to find an $E_r$ profile inside the plasma that fulfills the ambipolarity condition. Theoretically both, the electron-root and ion-root solution may co-exist. However, by starting the iteration loop with a positive $E_r$ value of +20 kV/m, finding the ion-root solution in the core prior to the electron-root can be avoided. The resulting $E_r$ profile is shown in black in figure 20. It agrees with the reflectometry data (given in red) but the profile is well outside the measurement uncertainties of the XICS system, given in blue. These measurement uncertainties do, however, only represent photon-noise. Systematic uncertainties in the system calibration are significantly larger (up to 50%) such that the DKES result might still be within the uncertainties of the XICS data.

The effect of the alternative $E_r$ on the $D_{nc}$ and $v_{nc}$ profiles is shown in figure 20b and c. Only data for the intermediate charge stage $Fe^{19+}$ is displayed to simplify the graph. The reduced $E_r$ profile from DKES yields slightly larger $D_{nc}$ values compared with the reference case, plotted in red, since the $\vec{E}_r \times \vec{B}$ rotation is smaller. Moreover, the amplitude of the calculated $v_{nc}$ profile becomes smaller due to the dependence of $v$ on $qE_r$.

In addition, the kinetic profiles ($n_e$, $T_e$ and $T_i$) have been varied in DKES according

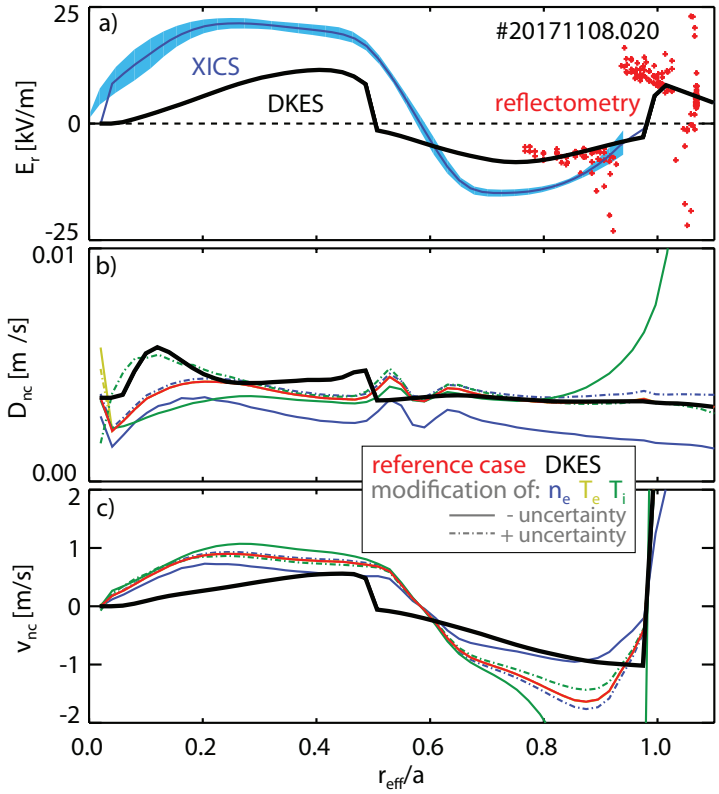


**Figure 20.** (a) Radial profiles $E_\mathrm{r}$ profile, as measured by XICS (blue) and reflectometry (red) compared with the one calculated with DKES (black). $D_\mathrm{nc}$ (b) and $v_\mathrm{nc}$ (c) neo-classical profiles from DKES, obtained when varying the input profiles. The $D_\mathrm{nc}$ and $v_\mathrm{nc}$ profiles in red correspond to the reference case and the ones in black to the $E_\mathrm{r}$ profile from DKES. The solid lines represent reduced values in the input profiles. The dashed lines represent increased values in the input profiles.

to the uncertainty boundaries plotted in figures 2 and 3. The resulting $D_\mathrm{nc}$ and $v_\mathrm{nc}$ profiles are given in figure 20 and do not exhibit a significant variation compared with the reference case (red). The neo-classical diffusion profiles of $Fe^{19+}$ remain below $0.01\,\mathrm{m}^2/\mathrm{s}$.

The modified $D_\mathrm{nc}$ and $v_\mathrm{nc}$ profiles have an effect on the predicted emissivities by STRAHL. However, the fitting algorithm can balance these effects by adjusting the anomalous diffusion profiles accordingly. The resulting $D$ profile when defining $E_\mathrm{r}$ by DKES is shown by the black, dashed line in figure 19. The profile is closer to the one found in section 4 and the $\mathcal{X}^2_r$ value is even lower than that of the reference case (red).

The effects of the modified kinetic profiles on the STRAHL fit-result are displayed in figure 19 as well. The solid lines correspond to reduced values in the kinetic profiles and the dashed ones represent increased profiles. The fit quality is indicated by the color-coded $\mathcal{X}^2_r$ values. As can be seen, changing the electron density or ion temperature does not strongly change the results. Instead, modifying the electron temperature profile can have a big impact on the fit-results since it affects the fractional abundance and PEC-coefficients in STRAHL. Both, reduced and increased electron temperature profiles result in a bad fit ($\mathcal{X}^2_r > 1.17$).

The impact of changing the neutral density profile, $n_0$, according to the boundaries plotted in figure 10, is displayed in purple lines in figure 19. Lowering the neutral density slightly improves the fit quality ($\mathcal{X}^2$=1.12) while increasing the neutral density yields $\mathcal{X}_r^2$=1.15 due to overly strong charge-exchange losses of the $Fe^{24+}$ stage.

For the fit-result plotted in orange in figure 19, the connection length, $L_c$, has been set to 50 m (solid lines) and $10^6$ m (dashed lines). This changes the loss time of particles into the divertor, $\tau_{div} = L_c/v_{flow}$ where $v_{flow}$ is the flow velocity. To match the experimental transport time when $L_c$ ($\tau_{div}$) is low (solid line), the fit finds higher $D_a$ values in the SOL. In contrast, it balances enhanced connection lengths by a lower SOL-diffusion (dashed line). Changing the $D_a$ values in the SOL does, however, affect the modeled time-delay and rise-time such that the fit quality degrades. It should be noted that changing $v_{flow}$ has a very similar effect (it is also related to $\tau_{div}$) such that a separate discussion is obsolete.

Finally, the timing of the LBO pulse, $t_0$, has been modified by ±1 ms. The resulting anomalous $D_a$ profiles are plotted in light blue in figure 19. The reduction of the LBO start-time in STRAHL (-1 ms) yields a lower diffusion profile in the SOL because a slower radial movement of the ablated Fe cloud is required to reach the emission layer of the Fe IX line in time. In contrast, increasing the start-time by +1 ms yields a higher diffusion value in the SOL.

In summary, a good representation of the spectrometer data is possible with $v_a$=0 even when modifying the input profiles or settings in STRAHL. The modification exhibits large variations in the resulting $D_a$ profiles, which indicates significant uncertainties in the obtained $D_a$ values. However, all profiles are well above the neo-classical level (even above 2.0 $m^2/s$) and are peaked off-axis.

## 6. DISCUSSION

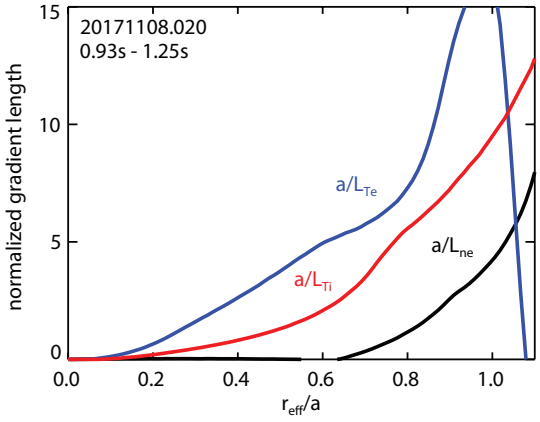


**Figure 21.** Radial profiles of the normalized gradient lengths of the electron temperature (blue), electron density (black) and ion temperature (red).

The optimization of W7-X with respect to the neo-classical transport makes it

easy to demonstrate the presence of anomalous impurity diffusion. The $D_{11}$ transport coefficient is small and not only results in small $D_{\rm nc}$ values but also in reduced $v_{\rm nc}$ profiles (see equation (1)). This situation is similar to tokamaks where radial transport is typically dominated by turbulence. In W7-X, turbulence has already been identified to affect the energy confinement time [43] which can be significantly smaller than expected from neo-classical theory. Also during the experiment discussed here, the energy confinement time, $\tau_{\rm E}$, is only 80 ms (estimated from the ratio of the plasma stored energy (0.4 MJ) and the applied heating power (5 MW) during steady state), which is much smaller than predicted by neo-classical transport modeling using the code NTSS [44].

In general, turbulent transport is expected in presence of strong gradients which drive the instabilities, developing turbulence. Figure 21 illustrates normalized gradient lengths $a/L$ which can be used to address the onset and strength of turbulent transport. In particular the normalized gradient lengths of the electron and ion temperature, $a/L_{T_e} = a\nabla T_e/T_e$ and $a/L_{T_i} = a\nabla T_i/T_i$ are large and increase towards the plasma edge. This profile shape is similar to what we observe for the anomalous impurity diffusion.

Also the absence of a strong anomalous convection velocity ($v_{\rm a} \approx 0$) agrees with the hypothesis of turbulent transport. From gyrokinetic theory, turbulent particle fluxes are ambipolar [45] such that the radial electric field, and hence the neo-classical transport should remain unchanged. Moreover, a direct turbulence-induced convection should be small, as reported recently by [6] (assuming quasi-linear theory).

## 7. SUMMARY

The impurity transport in H-plasmas of W7-X has been investigated in detail by analyzing the temporal behavior of Fe emission lines after a laser blow-off injection. Poor agreement is observed when comparing spectrometer measurements with STRAHL simulations that only consider neo-classical $D_{\rm nc}$ and $v_{\rm nc}$ profiles from DKES. In contrast, excellent agreement can be obtained when assuming additional anomalous $D_{\rm a}$ and $v_{\rm a}$ profiles in STRAHL, obtained using a least-squares fitting approach.

The resulting anomalous diffusion profile is well-defined through the time-delay and rise-time of 9 different line emissions after the LBO injection, it increases towards the edge and exhibits values above $1.0\,{\rm m}^2/{\rm s}$ (also verified by a scan of about 120,000 STRAHL runs). This is more than two orders of magnitude larger than the neo-classical expectation. Thanks to the optimization of W7-X with respect to neo-classical transport, the $D_{\rm nc}$ values are only in the range of $0.01\,{\rm m}^2/{\rm s}$. Also when modifying the kinetic profiles and $E_{\rm r}$ in DKES, the neo-classical diffusivities remain small which makes it robust and straightforward to conclude with anomalous impurity diffusion.

The conclusion whether there is an anomalous convection velocity is more difficult to draw. The fitted $v_{\rm a}$ profile is close to the neo-classical one and a fit with the assumption of $v_{\rm a}$=0 yields an almost equally good representation of experimental data (also within

the modeling uncertainties). However, it can be stated that the anomalous convection cannot be orders of magnitude larger than the neo-classical convection velocity. The observed impurity transport time (63 ms) restricts the minimum $v/D$ value close to the edge and the $v/D$ profile in the center is constrained by data from a soft X-ray imaging spectrometer (HR-XIS), measuring the Fe XXV emission profile at $r_{\mathrm{eff}}/a < 0.6$.

The observation of a strong anomalous diffusion towards the edge and low anomalous convection velocities supports the hypothesis of turbulent impurity transport. Turbulent transport is dominated by ordinary Fickian diffusion and is expected at off-axis positions due to its relation with normalized gradient lengths. Moreover, it is clear from a recent publication [43] that turbulent transport is present at W7-X since a significant contribution to the energy transport is observed.

With respect to the future exploitation of the stellarator concept, the observation of strong anomalous impurity transport is very promising. The anomalous transport could compensate for the inward-directed neo-classical convection velocity during core ion-root confinement conditions and might, thus, allow reactor-relevant long-pulse operation without accumulation.

## 8. ACKNOWLEDGMENTS

This work has been carried out within the framework of the EUROfusion Consortium and has received funding from the Euratom research and training programme 2014-2018 under Grant Agreement No. 633053. The views and opinions expressed herein do not necessarily reflect those of the European Commission.

[1] NEUHAUSER, J., Plasma Physics and Controlled Fusion **34** (1992) 2015.
[2] HELANDER, P. et al., Plasma Physics and Controlled Fusion **54** (2012) 124009.
[3] MAASSBERG, H. et al., Plasma Physics and Controlled Fusion **35** (1993) B319.
[4] BURHENN, R. et al., Nuclear Fusion **49** (2009) 065005.
[5] HELANDER, P. et al., Phys. Rev. Lett. **118** (2017) 155002.
[6] HELANDER, P. et al., Plasma Physics and Controlled Fusion **60** (2018) 084006.
[7] DUX, R. et al., Plasma Physics and Controlled Fusion **45** (2003) 1815.
[8] TAMURA, N. et al., Plasma Physics and Controlled Fusion **58** (2016) 114003.
[9] BEIDLER, C. et al., Fusion Technology **17** (1990) 148.
[10] KLINGER, T. et al., Plasma Physics and Controlled Fusion **59** (2017) 014018.
[11] LANGENBERG, A. et al., Nuclear Fusion **57** (2017) 086013.
[12] HIRSHMAN, S. P. et al., The Physics of Fluids **29** (1986) 2951.
[13] BEHRINGER, K., PLASMA PHYSICS AND FUSION TECHNOLOGY **19** (1987) 57.
[14] LABOMBARD, B., Plasma Science and Fusion Center Research Report (2001) PSFC.
[15] ANDREEVA, T., Technical Report IPPIII/270, Max-Planck-Institut fur Plasmaphysik, Garching (2002).
[16] RAHBARNIA, K. et al., Nuclear Fusion **58** (2018) 096010.
[17] BRUNNER, J., submitted to Journal of Instrumentation (2018).
[18] KRAMIDA, A. et al., (2018).
[19] WEGNER, T. et al., Review of Scientific Instruments **89** (2018) 073505.
[20] PASCH, E. et al., Review of Scientific Instruments **87** (2016) 11E729.
[21] BOZHENKOV, S. et al., Journal of Instrumentation **12** (2017) P10004.

[22] PABLANT, N. A. et al., Review of Scientific Instruments **83** (2012) 083506.
[23] PABLANT, N. A. et al., Physics of Plasmas **25** (2018) 022508.
[24] HINTON, F. L. et al., Rev. Mod. Phys. **48** (1976) 239.
[25] YOKOYAMA, M. et al., Nuclear Fusion **47** (2007) 1213.
[26] SATHEESWARAN, G. et al., Fusion Engineering and Design **123** (2017) 699 , Proceedings of the 29th Symposium on Fusion Technology (SOFT-29) Prague, Czech Republic, September 5-9, 2016.
[27] BIEL, W. et al., Review of Scientific Instruments **75** (2004) 3268.
[28] THOMSEN, H. et al., Journal of Instrumentation **10** (2015) P10015.
[29] BERTSCHINGER, G. et al., Review of Scientific Instruments **75** (2004) 3727.
[30] LANGENBERG, A. et al., Review of Scientific Instruments **89** (2018) 10G101.
[31] STEPHEY, L. et al., Review of Scientific Instruments **87** (2016) 11D606.
[32] GONCHAROV, P. et al., Plasma Fusion Res. (2007) 1132.
[33] SINHA, P. et al., Nuclear Fusion **58** (2018) 016027.
[34] SUMMERS, H. P., The ADAS User Manual, version 2.6 http://www.adas.ac.uk (2004).
[35] PUETTERICH, T., to be submitted to Nuclear Fusion (2018).
[36] HIRSHMAN, S. et al., Computer Physics Communications **43** (1986) 143 .
[37] PUIATTI, M. E. et al., Physics of Plasmas **13** (2006) 042501.
[38] SERTOLI, M. et al., Plasma Physics and Controlled Fusion **53** (2011) 035024.
[39] ODSTRCIL, T. et al., Plasma Physics and Controlled Fusion **60** (2018) 014003.
[40] DUX, R., IPP Report, Garching bei Mnchen: Max-Planck-Institut fr Plasmaphysik **10** (2004).
[41] SUDO, S., Plasma Physics and Controlled Fusion **58** (2016) 043001.
[42] NEUHAUSER, J. et al., Journal of Nuclear Materials **121** (1984) 194 .
[43] FUCHERT, G., submitted to Nuclear Fusion (2018).
[44] TURKIN, Y. et al., Physics of Plasmas **18** (2011) 022505.
[45] HELANDER, P., Reports on Progress in Physics **77** (2014) 087001.